

# LOW-RESOLUTION RECONSTRUCTION OF INTENSITY FUNCTIONS ON THE SPHERE FOR SINGLE-PARTICLE DIFFRACTION IMAGING

Julien Flamant<sup>†</sup>, Nicolas Le Bihan<sup>†\*</sup>, Andrew V. Martin<sup>‡</sup> and Jonathan H. Manton<sup>†</sup>

<sup>†</sup>: Department of Electrical and Electronic Engineering,

<sup>‡</sup>: ARC Centre for Advanced Molecular Imaging, School of Physics,  
The University of Melbourne, Melbourne, Victoria 3010, Australia.

## ABSTRACT

Single-particle imaging experiments using X-ray Free-Electron Lasers (XFEL) belong to a new generation of X-ray imaging techniques potentially allowing high resolution images of non-crystallizable molecules to be obtained. One of the challenges of single-particle imaging is the reconstruction of the 3D intensity function from only a few samples collected on a planar detector after the interaction of a free falling molecule and the X-ray beam. In this paper, we take advantage of the symmetries of the intensity function to propose an original low-resolution reconstruction algorithm based on an Expansion Maximization Compression (EMC) approach. We study the problem of adequate sampling of the rotation group via simulation to illustrate the potential of the approach.

**Index Terms**— Spherical Expectation Maximization Compression (EMC), Spherical Harmonic Transform (SHT), Sampling on  $SO(3)$ , Low-resolution reconstruction, Intensity functions, X-ray Free-Electron Laser (XFEL).

## 1. INTRODUCTION

Single particle imaging has been proposed as a method of determining the atomic structures of biomolecules that do not crystallize and, hence, have remained inaccessible to X-ray crystallography. X-ray Free-Electron Lasers (XFEL) produce pulses with up to a billion times higher peak brightness than synchrotron sources and have made it possible for the first time to collect X-ray diffraction from single protein molecules. These measurements are nevertheless extremely noisy because a single protein molecule is a very weak scatterer. The measurement is also destructive so each molecule can only be measured once. It is femtosecond time scale of the pulse which enables the diffraction to outrun the damage processes, so the measurement can be made at all. To obtain 3D information, multiple identical molecules are continuously injected into the path of the X-ray pulses. To gain 3D information and overcome low signal-to-noise, large datasets of millions of diffraction patterns are collected, exploiting the high repetition rates ( $> 100$  Hz) of X-ray laser sources. The drawback of continuous injection is that the orientation of each molecule is not controlled or known. To proceed with 3D imaging, the data needs to be assembled into a 3D intensity function by determining the unknown orientations. Currently the most popular solution is to determine relative orientation by analyzing the diffraction data and a number of algorithms have been proposed [17, 14, 6, 1, 15]. Here we focus on extending a Bayesian approach

known as the Expansion-Maximization-Compression (EMC) algorithm [10, 5] by reformulating it with spherical harmonics. Our goal is to develop an algorithm that permits the resolution and complexity of the problem to be readily scaled. We expect this to lead to more efficient algorithms for single particle imaging.

## 2. MATHEMATICAL PRELIMINARIES

Before presenting the measurement model, we first introduce the 3D intensity to be reconstructed. This intensity  $I(\mathbf{q})$  is related to the Fourier transform of the *electron density*  $\rho^{(\text{mol})}(\mathbf{r})$  of the biomolecule [2] the following way:

$$I(\mathbf{q}) = |F(\mathbf{q})|^2 I_0 \quad , \quad \text{with} \quad F(\mathbf{q}) = \int \rho^{(\text{mol})}(\mathbf{r}) \exp(i\mathbf{q} \cdot \mathbf{r}) d^3 \mathbf{r} \quad (1)$$

with  $I_0$  a scaling factor depending on the beam intensity, cross-section of the sample and the experimental geometry, and  $F(\mathbf{q})$  the *molecular transform*, where  $\mathbf{r}$  is the position variable used to locate atoms in the molecule and  $\mathbf{q}$  its dual variable (spatial frequency). The electron density  $\rho^{(\text{mol})}(\mathbf{r})$  is characteristic of each molecule and is the targeted quantity to be recovered, once the intensity is properly estimated, through a phase retrieval procedure [13]. In the present single-particle diffraction imaging setting, the intensity function exhibits the following properties: (i) it is a real-valued non-negative continuous function, (ii) it has the Friedel symmetry property  $I(\mathbf{q}) = I(-\mathbf{q})$ , (iii) it is a bandlimited function [2].

### 2.1. 3D reconstruction from 2D spherical shells

While the classical EMC algorithm works on the complete 3D intensity as a whole [10], our approach consists in attempting to reconstruct the intensity on spherical shells, before eventually re-assembling them. This is motivated by the possible use of harmonic analysis on spheres in the reconstruction step. Figure 1 presents the relation between the diffraction pattern and the observations available.

Circles on a diffraction pattern (Fig 1.A) correspond to intersections between the spherical 2D slice and a spherical shell  $s$ , with corresponding  $q_s$  radius on the diffraction pattern (Fig. 1.B and 1.C). Fig 1.D and 1.E show the circles associated to the same shell on different patterns. Fig 1.F and 1.G present the number of samples available for inner and outer shell. The reconstruction problem on a shell thus consists in building up an estimate of the intensity on a sphere from a few samples taking values on circles drawn (at random location) on that sphere. In the sequel, we present the case of

\*N. Le Bihan's research was supported by the ERA, European Union, through the International Outgoing Fellowship (IOF GeoSToSip 326176) program of the 7th PCRDP

two shells which illustrate well the complexity of the 3D intensity function: an inner shell (Fig 1.D) and an outer shell (Fig 1.E).

## 2.2. Efficient intensity representation using spherical harmonics

We denote by  $I^s(\Omega)$  the intensity on the shell  $s$  where the superscript  $s$  is for the radius  $q_s$  and  $\Omega$  is the position vector on the 2-sphere  $\mathbb{S}^2$ . Recall that the spherical harmonic functions  $Y_l^m$  form a complete orthonormal basis for functions in  $L^2(\mathbb{S}^2)$ . The intensity function  $I^s$  can then be expanded as

$$I^s(\Omega) = \sum_{l=0}^{L_s^{\text{lim}}-1} \sum_{m=-l}^l I_l^m(q_s) Y_l^m(\Omega), I_l^m(q_s) \triangleq \langle I^s, Y_l^m \rangle_{\mathbb{S}^2}, \quad (2)$$

where the spherical harmonic coefficients  $I_l^m(q_s)$  are obtained by projection onto the spherical harmonic functions with the standard inner product  $\langle \cdot, \cdot \rangle_{\mathbb{S}^2}$  on the 2-sphere. This set of coefficients is called the Spherical Harmonic Transform (SHT) of  $I^s(\Omega)$ . The spherical harmonic coefficients form an efficient representation of the intensity function; indeed since the intensity function is real-valued, we have the conjugation property  $I_l^{-m}(q_s) = (-1)^m \overline{I_l^m(q_s)}$  for  $m > 0$ . In addition, a key property of the intensity functions in X-ray scattering is that it fulfills the Friedel symmetry [18], which states that

$$I^s(\Omega) = I^s(-\Omega) \Leftrightarrow I_l^m(q_s) = 0, \forall l = 2p + 1, p \in \mathbb{N}. \quad (3)$$

This property induces that odd degrees of the SHT of the intensity vanish. This can be easily demonstrated using the parity property of spherical harmonics [16].

## 2.3. Measurement model

We propose hereafter a mathematical model of the measurement process, based on the single shell formulation. We consider a reference set of  $N$  points on the shell  $s$  denoted by  $\mathcal{D}^s$  such that:

$$\mathcal{D}^s \triangleq \{\mathbf{q}_i = (q_s, \Omega_i) | i = 1, 2, \dots, N\}, \quad (4)$$

where  $\Omega_i = (\phi_i, \theta(q_s)) \in [0, 2\pi) \times [0, \pi]$ . Examples of  $\mathcal{D}^s$  are displayed on Figure 1. The dependence of  $\theta$  on the radius  $q_s$  is a consequence of the scattering geometry, see [12, equation 2] for the explicit relation. To be consistent with the diffraction imaging context, the number of points  $N$  on the detector are also scaled as a function of  $q_s$ , such that:

$$N = \left\lceil \frac{2\pi q_s}{\Delta q} \right\rceil, \quad \phi_i = \frac{2\pi}{N} i, i \in \{0, 1, \dots, N-1\}, \quad (5)$$

where  $\lceil \cdot \rceil$  denotes the ceiling function, and  $\Delta q$  is the reciprocal space pixel size. The analogy with the single-particle experiment is as follows. Each observation  $k$  corresponds to a random rotation  $\mathcal{R}_k$  of the molecule, and on the shell  $s$  the circle intersection is given by:

$$\mathcal{D}_{\mathcal{R}_k}^s \triangleq \{\mathcal{R}_k \cdot \mathbf{q}_i | i = 1, 2, \dots, N\}. \quad (6)$$

Random rotations  $\mathcal{R}_k$  are assumed to be distributed uniformly on  $SO(3)$  as free falling particules have no preferred orientation. Each measurement  $\mathbf{y}_k = (y_{1k}, y_{2k}, \dots, y_{Nk})^T$  consists in a set of  $N$  samples  $y_{ik}$  given by:

$$y_{ik} = \mathcal{P}\{I^s(\mathcal{R}_k \cdot \mathbf{q}_i)\}, \quad \mathcal{R}_k \sim \mathcal{U}[SO(3)]. \quad (7)$$

Here  $\mathcal{P}\{x\}$  denotes the Poisson distribution of parameter  $x$ . Three Poisson measurements for  $k = 1, 2, 3$  in both the inner and outer shells are displayed in Figure 1E and 1F. They illustrate the low number of samples  $k$  with respect with the *measurement points*  $N$ , especially in the outer shell.

## 3. SPHERICAL EMC ALGORITHM

We develop here an extension of the Expansion-Maximization-Compression (EMC) algorithm [10] in a spherical setting. This reformulation is motivated by: (i) the intrinsic geometry of the scattered intensity function; (ii) the use of spherical harmonics to obtain low-resolution reconstructions.

The EMC algorithm relies on an Expectation-Maximization (EM) algorithm [3], with two extra Expansion and Compression steps, as explained below. We reproduce some material from [10], and transpose the algorithm to the spherical setting.

### 3.1. Presentation

The spherical EMC algorithm proposed here consists of an update rule  $I_l^m(q_s) \rightarrow \tilde{I}_l^m(q_s)$  of the low-degree spherical harmonic coefficients of the intensity.

The EMC algorithm restores the missing orientation information from the measurements  $k$  by introducing a *tomographic grid*, which is defined by successive rotations of the reference measurement coordinates  $\mathbf{q}_i$ . Precisely, given a uniform deterministic sampling set  $\mathcal{X} \subset SO(3)$ , the tomographic grid points are defined by  $\mathbf{q}_{ij} = \mathcal{R}_j \mathbf{q}_i$ ,  $\mathcal{R}_j \in \mathcal{X}$ . A tomographic intensity is a set  $I_{ij} = I(\mathbf{q}_{ij})$ , where the intensity is evaluated at the tomographic grid points. The tomographic intensity model is at the heart of the EMC algorithm, as we now explain.

Under the assumption that the measurements are independent, the joint conditional probability for a rotation  $j$  and measurement  $k$  reads:

$$R_{jk} \triangleq P(\mathbf{y}_k | \{I_{ij}\}_{i=1, \dots, N}) = \prod_{i=1}^N (I_{ij})^{y_{ik}} \exp(-I_{ij}) \quad (8)$$

where an irrelevant  $j$ -independent factor has been omitted. The probability  $P_{jk}$  that the observation  $k$  corresponded to the rotation  $j$  is given by the normalization of  $R_{jk}$

$$P_{jk} = \frac{R_{jk}}{\sum_{j=1}^M R_{jk}}, \quad (9)$$

where, as opposed to [10], the weights  $w_j$  have disappeared since the rotation sampling set  $\mathcal{X}$  is chosen such that the weights are uniform. This point is discussed further in section 3.3. The total likelihood function  $\mathcal{L}$  is given by

$$\mathcal{L}(\tilde{I}_{ij} | I_{ij}, \mathbf{y}_k) = \sum_{k=1}^K \sum_{j=1}^M P_{jk} \sum_{i=1}^N (y_{ik} \log \tilde{I}_{ij} - \tilde{I}_{ij}). \quad (10)$$

Simple calculation therefore leads to the Maximization step:

$$(\mathbf{M}) : I_{ij} \rightarrow \tilde{I}_{ij} = \frac{\sum_{k=1}^K P_{jk} y_{ik}}{\sum_{k=1}^K P_{jk}}. \quad (11)$$

One can note that the tomographic grid is indeed a redundant model of the true intensity  $I$ , since it is possible to find  $(i', j') \neq (i, j)$  such

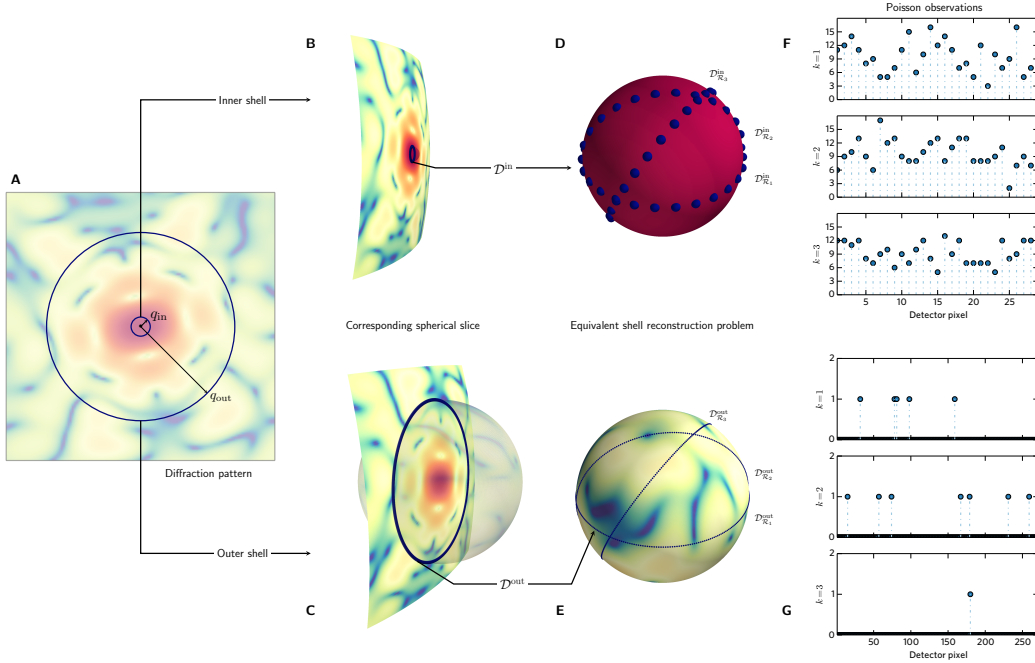


**Fig. 1.** Spherical shell equivalency for single-particle imaging. **A:** typical diffraction pattern, with two shells labelled (inner and outer). **B** and **C:** corresponding spherical slices through the shell intensity function. **D** and **E:** Equivalent shell reconstruction problem using 1D circular sampling points. **F:** and **G** Corresponding Poisson samples for the sampling locations labeled on **D** and **E**.

that the tomographic points  $\mathbf{q}_{ij}$  and  $\mathbf{q}_{i'j'}$  are really close from each other. Therefore we need to restore the consistency of the model, and this is done in the Compression step.

In the spherical setting, the Compression step corresponds to two distinct steps. First, the tomographic model has to be compressed to a regular spherical grid  $\mathcal{G}$ , and thus the spherical harmonic coefficients can be retrieved with the Spherical Harmonic Transform (SHT):

$$(C) : \tilde{I}_{ij} \rightarrow \tilde{I}_{\mathcal{G}}(q_s) \rightarrow \tilde{I}_l^m(q_s) \quad (12)$$

The Expansion step is the reverse part, where we first apply the inverse SHT to get the intensity on the grid  $\mathcal{G}$ , and we interpolate to get the tomographic intensity model

$$(E) : I_l^m(q_s) \rightarrow I_{\mathcal{G}}(q_s) \rightarrow I_{ij}. \quad (13)$$

The implementation of C and E steps are discussed in the next section. The EMC algorithm performs successively the E,M,C steps until convergence is achieved. The use of spherical EMC raises two issues: how to sample the sphere (*i.e.* choose a grid  $\mathcal{G}$  where the intensity is estimated) for the reconstruction of the intensity at a given resolution degree  $L < L_s^{\text{lim}}$ , and how the rotation sampling set  $\mathcal{X}$  has to be chosen. The following sections address these problems.

### 3.2. Low-resolution intensity functions and compatible grid

We are interested in the reconstruction of low-resolution intensity models, that is we look at models which read

$$I^s(\Omega) = \sum_{l=0}^{L-1} \sum_{m=-l}^l I_l^m(q_s) Y_l^m(\Omega) \quad (14)$$

where  $L < L_s^{\text{lim}}$  is the bandlimit of the reconstruction. Numerous sampling theorems on the sphere have been proposed to date [4, 9, 11]. Our work uses the HEALPix framework [7] to represent bandlimited functions on the sphere. This grid exhibits a hierarchical structure, equal-area partition of the sphere and was originally developed for full-sky measurements of the Cosmic Microwave Background (CMB). The resolution of the grid is controlled by the parameter  $n_{\text{side}}$ , such that the number of pixels  $n_{\text{pix}}$  reads

$$n_{\text{pix}} = 12n_{\text{side}}^2, \quad n_{\text{side}} = 1, 2, 4, 8, \dots \quad (15)$$

The HEALPix sampling scheme lacks an exact quadrature formula on the sphere, however it provides a good approximation of integrals of  $L$ -bandlimited functions provided that [7]

$$L \leq 2n_{\text{side}} + 1 \text{ with weights } w_i = \frac{4\pi}{n_{\text{pix}}}, \quad i = 1, 2, \dots, n_{\text{pix}}. \quad (16)$$

The Compression step is done as follows. We first determine the tomographic points  $\mathbf{q}_{ij}$  belonging to each HEALPix pixel. Then the intensity value on this pixel is given by Inverse Distance Weighting between the respective  $\mathbf{q}_{ij}$  and the pixel center. The coefficients  $I_l^m(q_s)$  are then computed up to degree  $L - 1$  as given by the sampling theorem (16). The Friedel symmetry is restored by canceling the coefficients for odd values of  $l$ . The Expansion step is done by the successive expansion of the coefficients  $I_l^m(q_s)$  to obtain  $I_{\mathcal{G}}(q_s)$ , then by computation of the tomographic intensities by bilinear interpolation on the sphere.

### 3.3. Rotation group sampling sets for low-resolution

Several uniform deterministic sampling sets on  $SO(3)$  have been defined in [8] based on the tensor product  $\mathbb{S}^2 \times \mathbb{S}^1$  structure of the

rotation group. The idea is to build sampling sets from Platonic solids in  $\mathbb{R}^3$ , namely in our case from the tetrahedron and the icosahedron. This leads to the definition of the associated rotation groups, tetrahedron-based  $\mathcal{X}_T$  and icosahedron-based  $\mathcal{X}_I$ , with respective sizes  $|\mathcal{X}_T| = 12$  and  $|\mathcal{X}_I| = 60$ . We note that the icosahedron-based sampling has the same size as the smallest sampling set proposed in the original EMC paper [10].

Since we are interested in low-resolution models, we would like to give a criterion to choose the appropriate rotation sampling set. It seems indeed that an over-resolved rotation sampling set is unnecessary in the estimation of low-resolution models. A quantification of the resolution of a sampling set can be given by considering the quadrature degree on  $SO(3)$  associated with this sampling set. The quadrature degree is defined as the maximum degree  $l$  of the Wigner-D functions which can be exactly integrated over  $SO(3)$ . It can be shown that the sampling sets  $\mathcal{X}_T$  and  $\mathcal{X}_I$  define indeed quadrature rules with equal weights and respective degrees  $\text{deg } \mathcal{X}_T = 2$  and  $\text{deg } \mathcal{X}_I = 5$ , see [8].

The strong connection between  $SO(3)$  and the sphere  $\mathbb{S}^2$  leads to a simple choice criterion for the rotation sampling set given the bandlimit  $L$  of the reconstruction. Precisely, we consider that the quadrature degree of the sampling set should be larger than the maximum degree in the spherical harmonic decomposition of the low-resolution reconstruction, that is

$$\text{deg } \mathcal{X} \geq L - 1. \quad (17)$$

It is straightforward to see that for the first resolution  $L = 3$  both  $\mathcal{X}_T$  and  $\mathcal{X}_I$  fulfill the criterion (17), whereas only  $\mathcal{X}_I$  is available for the second resolution  $L = 5$ . Since computation time is critical, for  $L = 3$  the rotation sampling  $\mathcal{X}_T$  set will be chosen.

#### 4. RESULTS

Results are presented on an inner shell and a outer shell as depicted in Fig. 1. As a reconstruction error metric, we use  $\varepsilon_l = (|\hat{E}_l - E_l|)/E_l$ , where  $\hat{E}_l$  and  $E_l$  are respectively the estimated and theoretical energy of degree  $l$ , defined by  $E_l = \sum_{m=-l}^l |I_l^m|^2$ . This is a rotation invariant quantity. The true intensity function is computed from the Bence-Jones protein structure (pdb entry: 1REI). To avoid any bias the true intensity is computed on a large spherical grid such that  $n_{\text{side}} = 128$ . For each  $K$ , we simulate  $K$  uniform random rotations  $\mathcal{R}_k$  to obtain the sample points  $\mathcal{D}_{\mathcal{R}_k}^s$ , and the measurements  $\mathbf{y}_k$  are obtained by the Poisson model. The average behavior of the algorithm is obtained by *quasi*-Monte Carlo method, and with  $N_{\text{MC}} = 100$  runs.

In Figure 2, one can see the convergence of the estimation of the SH coefficients for  $L = 3$  and  $L = 5$  as a function of the number of patterns. For the inner shell, the relative error is low for  $l = 0, 2$  in both cases ( $n_{\text{side}} = 1, \mathcal{X}_T$ ) and ( $n_{\text{side}} = 2, \mathcal{X}_I$ ). The case  $l = 4$  is special (large error) but the relative contribution of this coefficients is very low in the reconstruction. For the outer shell (Fig 2, bottom row), convergence is achieved slower (due to sparse measurements) and aliasing issues arising from an energy distribution much wider. The aliasing phenomenon is actually univertable, and a consequence of the sub-Nyquist sampling on the regular grid  $\mathcal{G}$ .

Figure 3 presents reconstructions from the set of coefficients estimated in the case  $K = 400$  observations, with a grid  $n_{\text{side}} = 128$ . One can see that orientation is not preserved as reconstruction is performed independently on shells. As can be seen for  $L = 3$  of the

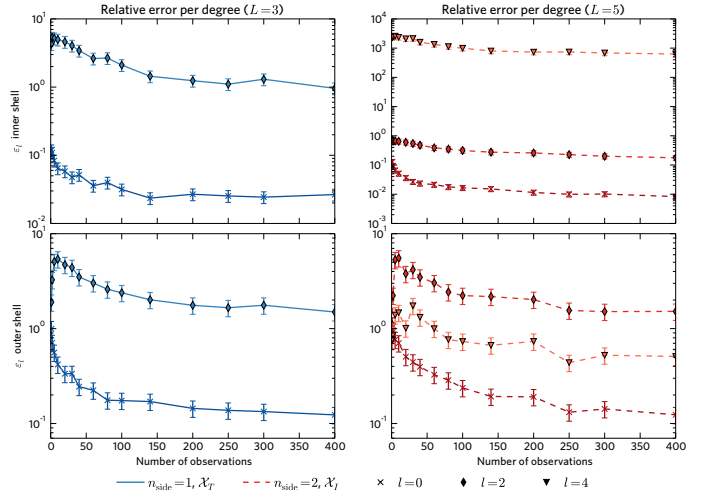


**Fig. 2.** Average relative error convergence with respect to the number of patterns for the inner and outer shell, for  $L = 3$  (left) and  $L = 5$  (right).

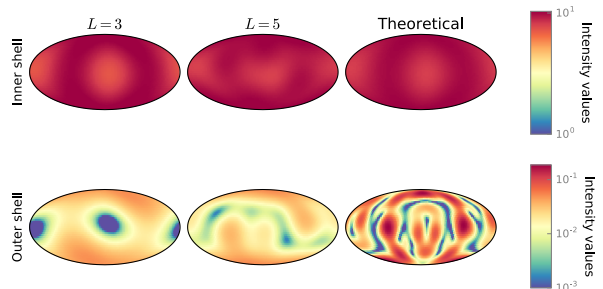


**Fig. 3.** Inner and outer shell low-resolution reconstructions for  $L = 3, 5$  and  $K = 400$ . Log-scale thresholded colormaps.

outer shell in Figure 3, SHT can lead to negative values in the reconstructed intensity. This is a drawback of using SHT as intensity should always be positive. As expected the low resolution estimation fits quite well the theoretical inner shell, whereas more degrees would be needed in the outer shell to obtain a good estimate.

One of the advantages of using the SHT also comes from the oversampling at will (here we used  $n_{\text{side}} = 128$ ). It should allow much more flexibility for phase retrieval algorithms to be performed after intensity reconstruction.

#### 5. CONCLUSIONS & PERSPECTIVES

Taking advantage of the symmetries of intensity functions can lead to low-resolution estimator which is not tractable using the classical EMC technique used in single-particle imaging. The proposed spherical version allows reconstruction of the intensity by successive shells thanks to an efficient SHT representation and with the desired resolution and the associated optimal size of grid. Future work will consist in assembling the reconstructed shells which are subject to relative rotations and to study alternate bases for the reconstruction.

## 6. REFERENCES

- [1] H. N. Chapman. X-ray imaging beyond the limits. *Nature materials*, 8(4):299–301, 2009.
- [2] H. N. Chapman, A. Barty, S. Marchesini, A. Noy, S. P. Hau-Riege, C. Cui, M. R. Howells, R. Rosen, H. He, J. C. Spence, et al. High-resolution ab initio three-dimensional x-ray diffraction microscopy. *JOSA A*, 23(5):1179–1200, 2006.
- [3] A. P. Dempster, N. M. Laird, and D. B. Rubin. Maximum likelihood from incomplete data via the EM algorithm. *Journal of the royal statistical society. Series B (methodological)*, pages 1–38, 1977.
- [4] J. R. Driscoll and D. M. Healy. Computing Fourier transforms and convolutions on the 2-sphere. *Advances in applied mathematics*, 15(2):202–250, 1994.
- [5] V. Elser. Noise limits on reconstructing diffraction signals from random tomographs. *Information Theory, IEEE Transactions on*, 55(10):4715–4722, 2009.
- [6] R. Fung, V. Shneerson, D. K. Saldin, and A. Ourmazd. Structure from fleeting illumination of faint spinning objects in flight. *Nature Physics*, 5(1):64–67, 2009.
- [7] K. M. Gorski, E. Hivon, A. Banday, B. D. Wandelt, F. K. Hansen, M. Reinecke, and M. Bartelmann. HEALPix: a framework for high-resolution discretization and fast analysis of data distributed on the sphere. *The Astrophysical Journal*, 622(2):759, 2005.
- [8] M. Gräf and D. Potts. Sampling sets and quadrature formulae on the rotation group. *Numerical Functional Analysis and Optimization*, 30(7-8):665–688, 2009.
- [9] Z. Khalid, R. Kennedy, J. D. McEwen, et al. An optimal-dimensionality sampling scheme on the sphere with fast spherical harmonic transforms. *Signal Processing, IEEE Transactions on*, 62(17):4597–4610, 2014.
- [10] N.-T. D. Loh and V. Elser. Reconstruction algorithm for single-particle diffraction imaging experiments. *Physical Review E*, 80(2):026705, 2009.
- [11] J. D. McEwen and Y. Wiaux. A novel sampling theorem on the sphere. *Signal Processing, IEEE Transactions on*, 59(12):5876–5887, 2011.
- [12] D. Saldin, V. Shneerson, R. Fung, and A. Ourmazd. Structure of isolated biomolecules obtained from ultrashort x-ray pulses: exploiting the symmetry of random orientations. *Journal of Physics: Condensed Matter*, 21(13):134014, 2009.
- [13] Y. Shechtman, Y. C. Eldar, O. Cohen, H. N. Chapman, J. Miao, and M. Segev. Phase retrieval with application to optical imaging: a contemporary overview. *Signal Processing Magazine, IEEE*, 32(3):87–109, 2015.
- [14] V. Shneerson, A. Ourmazd, and D. Saldin. Crystallography without crystals. i. the common-line method for assembling a three-dimensional diffraction volume from single-particle scattering. *Acta Crystallographica Section A: Foundations of Crystallography*, 64(2):303–315, 2008.
- [15] D. Starodub, A. Aquila, S. Bajt, M. Barthelmeß, A. Barty, C. Bostedt, J. D. Bozek, N. Coppola, R. B. Doak, S. W. Epp, et al. Single-particle structure determination by correlations of snapshot x-ray diffraction patterns. *Nature communications*, 3:1276, 2012.
- [16] M. Tinkham. *Group theory and quantum mechanics*. Courier Corporation, 2003.
- [17] M. Walczak and H. Grubmüller. Bayesian orientation estimate and structure information from sparse single-molecule X-ray diffraction images. *Physical Review E*, 90(2):022714, 2014.
- [18] B. E. Warren. *X-ray Diffraction*. Courier Corporation, 1969.